In-situ construction of 2D/1D $Bi_2O_2CO_3$ nanoflake/S-doped g-C_3N_4 hollow tube hierarchical heterostructure with enhanced visible-light photocatalytic activity

Zhifeng Liu, Jing Huang, Binbin Shao, Hua Zhong, Qinghua Liang, Qingyun He, Ting Wu, Yuan Pan, Zan Peng, Xingzhong Yuan, Yang Liu, Chenhui Zhao

PII: S1385-8947(21)02353-6
DOI: https://doi.org/10.1016/j.cej.2021.130767
Reference: CEJ 130767

To appear in: *Chemical Engineering Journal*

Received Date: 4 March 2021
Revised Date: 11 May 2021
Accepted Date: 5 June 2021

Please cite this article as: Z. Liu, J. Huang, B. Shao, H. Zhong, Q. Liang, Q. He, T. Wu, Y. Pan, Z. Peng, X. Yuan, Y. Liu, C. Zhao, In-situ construction of 2D/1D $Bi_2O_2CO_3$ nanoflake/S-doped g-C_3N_4 hollow tube hierarchical heterostructure with enhanced visible-light photocatalytic activity, *Chemical Engineering Journal* (2021), doi: https://doi.org/10.1016/j.cej.2021.130767

In-situ construction of 2D/1D $Bi_2O_2CO_3$ nanoflake/S-doped g-C_3N_4 hollow tube hierarchical heterostructure with enhanced visible-light photocatalytic activity

Zhifeng Liu [a,1,*], Jing Huang [a,1], Binbin Shao [a,1], Hua Zhong [a,b,*], Qinghua Liang [a], Qingyun He [a], Ting Wu [a], Yuan Pan [a], Zan Peng [a], Xingzhong Yuan [a], Yang Liu [a], Chenhui Zhao [a]

[a] College of Environmental Science and Engineering, Hunan University and Key Laboratory of Environmental Biology and Pollution Control (Hunan University), Ministry of Education, Changsha 410082, P.R. China

[b] State Key Laboratory of Water Resources and Hydropower Engineering Science, Wuhan University, Wuhan, Hubei 430072, P.R. China

* Corresponding authors at:

[a] College of Environmental Science and Engineering, Hunan University and Key Laboratory of Environmental Biology and Pollution Control (Hunan University), Ministry of Education, Changsha 410082, P.R. China

E-mail: zhifengliu@hnu.edu.cn (Z. Liu)

E-mail: zhonghua21cn@126.com (H. Zhong)

[1] The authors contribute equally to this paper.

Abstract

The construction of heterojunction photocatalysts was considered to be an effective strategy to tackle refractory pollutants. However, most of the reported composites lacked precise control of their morphology, resulting in unsatisfactory catalytic activity. In this work, we successfully fabricated sulfur doped g-C_3N_4 hollow tubes (SCN) via molecular self-assembly, and then grew the $Bi_2O_2CO_3$ nanoflakes (BOC) in situ parallel on the surface of SCN to construct 2D/1D interfacial phase. Within 30 min visible light irradiation, the robust BOC/SCN-3 heterostructure showed considerable improvement for tetracycline degradation (82.6%) compared with individual components. This enhanced photocatalytic performance derived from the synergistic effect of S doping and heterojunction interface contact. The tubular structure formed by S doping not only narrowed the bandgap and thus boosting the visible light harvesting of CN, but also promoted electrons to travel along the 1D longitudinal and radial directions. In addition, the built-in electric field between BOC and SCN effectively achieved the spatial separation of electron-hole pairs. Mechanism analysis revealed that the h^+ and $\bullet O_2^-$ radicals played the dominating contribution in the photocatalytic process, and a possible Z-scheme mechanism was proposed. It was expected that such design route could provide a new perspective on hierarchical heterostructure for pollutant removal.

Keywords: Photocatalysis, $Bi_2O_2CO_3$, S-doped hollow tubular g-C_3N_4, Z-scheme hierarchical heterostructure, Pollutant removal.

1. Introduction

With the improvement of health awareness and the growth of drug production, antibiotics have been widely applied in the field of healthcare, animal husbandry and aquaculture [1, 2]. Especially for broad-spectrum tetracycline, it has become one of the most frequently used antibiotics due to its strong antibacterial effect and low price [3-5]. However, tetracycline with stable structure cannot be completely metabolized by human or animal body so that it is constantly discharged into water in various forms, posing a threat to the ecological environment [6, 7]. Therefore, technologies with green and high efficiency to remove residual antibiotics in the water are urgently needed.

Photocatalytic technology has shown great potential in the treatment of refractory organic pollutants [8-10]. It utilizes solar energy to degrade antibiotic macromolecules into H_2O and CO_2 or small molecules. Generally, the strong redox ability of a semiconductor photocatalyst is related to the high potential of the valence band and conduction band, but the enlarged band gap will make it difficult for photogenerated carriers to be activated by visible light. One of the effective strategies to solve the above problems is to combine two or more semiconductor materials to construct heterostructure photocatalysts, which can not only expand the light-response range, but also promote the separation of photogenerated electron-hole pairs [11-14]. At present, the common heterostructure types include porous structures, core-shell structures and hierarchical structures [15-17].

Among diverse semiconductor photocatalysts, as a member of the

Aurivillius-related oxide family, $Bi_2O_2CO_3$ characterized by the alternating $Bi_2O_2^{2+}$ and CO_3^{2-} layers has attracted the attention of researchers [18-20]. This unique layered stacked structure can form a spontaneous built-in electric field in the semiconductor, which has been proven to enhance the charge separation efficiency. However, the large band gap (about 3.3 eV) renders pristine $Bi_2O_2CO_3$ semiconductor only to absorb ultraviolet light and thus greatly limiting its practical photocatalytic applications. In order to enhance the adsorption of visible light, a feasible approach is to couple $Bi_2O_2CO_3$ with other narrow-band-gap semiconductors, g-C_3N_4 is considered as an excellent candidate due to its adjustable band gap and suitable energy band matching [21-23]. Hence, a series of $Bi_2O_2CO_3$/g-C_3N_4-based composites have been constructed by different synthesis methods and applied for environmental remediation (Table 1) [24-26]. However, most of the reported composites lacked precise control of their morphology, which resulted in the reduction of surface area and active sites as well as the accelerated recombination of photogenerated electron-hole pairs, thereby inhibiting the interface reaction.

Inspired by the preceding discussion, we designed a novel 2D/1D $Bi_2O_2CO_3$ nanoflake/S-doped g-C_3N_4 hollow tube hierarchical heterostructure via hydrothermal method. The addition of surfactant cetyltrimethylammonium bromide (CTAB) caused $Bi_2O_2CO_3$ internal layered structure to grow at different axes, resulting in the formation of 2D nanostructure [27], where the number of active sites were distributed on the surface and a shorter diffusion path could accelerate the separation of excitons. In addition, through the self-assembly of melamine and trithiocyanuric acid, the morphology control and element doping of g-C_3N_4 were achieved simultaneously. Compared with the bulk counterpart, the well-defined 1D hollow tubular structure with high length-to-diameter ratio could not only enhance the light-harvesting ability, but also possess rapid and direct electronic transport pathway [28]. Moreover, the doping of S element could adjust the energy band structure of g-C_3N_4 to reduce the electron excitation energy [29, 30]. Herein, $Bi_2O_2CO_3$ nanoflakes grew in situ on the surface of S-doped g-C_3N_4 hollow tubes with tight heterojunction interface, and the composites displayed highly photocatalytic tetracycline hydrochloride (TCH) removal efficiency within 30 min. This work indicated that the rational construction of 2D/1D hierarchical heterojunction photocatalyst could maximize the multidimensional and synergistic effects of 2D and 1D materials and reinforce the photocatalytic activity.

2. Experimental section

2.1. Materials

Melamine ($C_3H_6N_6$), trithiocyanuric acid ($C_3H_3N_3S_3$), bismuth nitrate hydrate ($Bi(NO_3)_3 \cdot 5H_2O$), sodium carbonate (Na_2CO_3), CTAB ($C_{19}H_{42}BrN$) and tetracycline hydrochloride were purchased from Alfa or Sinopharm Chemical Reagent Co., Ltd. (Shanghai, China). All the chemicals were analytic pure and used directly. The deionized water (18.25 $M\Omega\ cm^{-1}$) was applied throughout the whole experiments.

2.2. Photocatalyst preparation

The S-doped g-C_3N_4 (SCN) was prepared according to our previous works with subtle alteration [31]. In a typical procedure, 0.6 mmol melamine and 0.8 mmol trithiocyanuric acid were dissolved in 70 mL deionized water solution under vigorous magnetic stirring for 3 h. Then, the solution was transferred to Teflon lined autoclave and heated at 120 °C for 5 h to promote molecular self-assembly. Next, the resulting precipitate was filtered with deionized water washing and dried at 60 °C to obtain precursor. Subsequently, the precursor was calcined at 550 °C (2.3 °C min^{-1} rising rate) and kept for 4 h under N_2 atmosphere. For comparison, the bulk g-C_3N_4 (CN) sample was prepared by directly calcining melamine.

For the preparation of $Bi_2O_2CO_3$/S-doped g-C_3N_4 (BOC/SCN) composites, 1 mmol $Bi(NO_3)_3 \cdot 5H_2O$ and a certain amount of SCN were added to 20 mL of 1 mol L^{-1} HNO_3 aqueous solution (denoted as solution A). At the same time, 5 mmol Na_2CO_3 and 0.1 g CTAB were dissolved in 60 mL deionized water (denoted as solution B). Solution A and B were subjected to stir for 30 min, respectively, and then solution A was slowly poured into solution B accompanied by steady stirring. After 30 min of stirring, the resulting suspension was transferred to Teflon lined autoclave and heated at 60 °C for 24 h. Finally, the pale-yellow powder was collected by filtered, washed with deionized water for three times and dried at 60 °C for overnight. According to the mass ratios of SCN to BOC (25 %, 20 %, 15 %, 10 %), the obtained samples were recorded as BOC/SCN-X (X = 1, 2, 3, 4), respectively. The pristine BOC was synthesized under the same conditions except the addition of SCN. The synthetic process of BOC/SCN was illustrated in Scheme 1.

3. Results and discussion

3.1. Morphology structure

The morphology of the as-prepared samples was characterized by SEM and

TEM. As depicted in Fig. 1a, CN exhibited typical stacked sheets, and SCN presented obvious hollow tubular structure with a diameter of 1-2 μm (Fig. 1b), which demonstrated that the self-assembly of melamine and trithiocyanic acid promoted the formation of 1D structure and S doping changed the morphology of CN substantially. In addition, the SEM image of BOC (Fig. 1c) showed that BOC was composed by a great number of nanoflakes (about 30 nm thickness). After coupling with SCN, the morphology of BOC was not destroyed or changed, and the nanoflakes grew parallel in situ on the surface of SCN (Fig. 1d-e). This parallel growth increased the contact area between semiconductors and facilitated the transfer of electrons [32], which laid the foundation for efficient photodegradation performance of composite. The SEM-EDX element mappings (Fig. 1f) further confirmed that C, N, O, S and Bi elements were distributed in the composite, and the specific mass and atomic ratios were shown in Fig. S1.

The detailed microstructure of the samples was obtained by TEM and HRTEM. Consistent with SEM results, SCN and BOC (Fig. 2a-b) exhibited hollow tubular structure and nanoflake structure, respectively, and these two components were intimately anchored to fabricate the heterojunction (Fig. 2c). The HRTEM image of BOC/SCN-3 showed a region with clear lattice fringes with approximately 0.232 nm lattice spacing (Fig. 2d), which corresponded to the (110) crystal planes of BOC [33], suggesting that the BOC component in composite maintained a high degree of crystallinity.

The N_2 adsorption-desorption isotherms were displayed in Fig. 3a and the porous parameters were shown in Table 2. It clearly presented that all samples were of type III isotherm. Obviously, the hysteresis loop of BOC/SCN-3 was broadened than pristine BOC, suggesting the presence of more mesopores and macropores. The BET surface areas were calculated to be 16.328 m^2 g^{-1} and 28.846 m^2 g^{-1} for BOC and BOC/SCN-3, respectively, and the corresponding pore volume from BJH desorption were 0.089 cm^3 g^{-1} and 0.108 cm^3 g^{-1}, respectively. The enhanced surface area and pore volume of composite derived from the construction of 2D/1D heterojunction and relatively dispersed BOC nanoflakes, which allowed greater diffusion of antibiotic molecules and increased the active sites of catalyst.

3.2. Crystal and chemical structure

The crystal structures of the as-prepared samples were presented by XRD patterns in Fig. 3b. The CN possessed two characteristic peaks at 13.0° ((100) facet) and 27.6° ((002) facet), which could be assigned to the in-plane structure packing and interlaminar stacking of CN, respectively [34, 35]. After doping with sulfur, the intensity of these two main peaks became weaker, indicating that the crystallinity of CN was destroyed and the strength of intermolecular hydrogen bonding interaction was reduced, which owing to the size-dependent property of hollow structure [36]. All diffraction peaks of BOC were highly matched with the standard PDF card of tetragonal $Bi_2O_2CO_3$ (JCPDS #41-1488) without other impurity diffraction peaks appearing [37], suggesting that the well-crystallized sample was formed. After hybridization with SCN, the XRD patten of BOC/SCN-3 still maintained the similarity with the pristine BOC, which meant that SCN did not affect the crystal structure of BOC. Notably, the (002) diffraction peak for BOC was slightly weakened in BOC/SCN-3, it was possible caused by the in situ growth of the BOC (001) facet on the SCN (002) facet [25]. In addition, no crystal phases of SCN were found in composite, this might be due to the amorphous state and low content of SCN [38]. In order to clarify the actual mass ratios of SCN to BOC, the contents of BOC in composites were performed by ICP-OES. In detail, the mass ratios of BOC in sample BOC/SCN-1, BOC/SCN-2, BOC/SCN-3, BOC/SCN-4 were confirmed to be 77.48%, 81.35%, 84.62% and 89.59%, respectively. The result indicated that the actual mass ratios of SCN to BOC (29.06%, 22.93%, 18.18% and 11.62%) were slightly higher than experimental designed values (25%, 20%, 15% and 10%), which might be due to the incomplete formation of BOC during the hydrothermal reaction.

Fig.3c presented the FTIR spectra of pure components and heterostructured composites. The intensive peaks of CN at 800 and 887 cm^{-1} were accounted for the bending mode of the triazine units and the deformation mode of N-H, respectively [39]. A series of absorption peaks at a range of 1130 to 1620 cm^{-1} were assigned to the typical stretching vibration of C=N (sp^3) and C-N (sp^2). Besides, a broad peak observed at 3000-3500 cm^{-1} could be attributed to the N-H stretching vibration [40]. The similar FTIR spectrum was also detected in SCN without clear stretching vibration of S bond, which might be because the low S content causing the corresponding vibration peaks to be insignificant, and further confirming that S doping did not affect the chemical structure of pristine CN. As for BOC, the absorption peak at 539 cm^{-1} was belonged to the Bi-O stretching vibration [24]. The bending mode and the antisymmetric vibration mode of CO_3^{2-} were characterised at 845 and 1370 cm^{-1}, respectively. In addition, the peaks in the region of 2800-3600 cm^{-1} were basically known as the O-H vibration of adsorbed water [26, 41]. All these peaks of SCN and BOC were existed in the composites, and no impurity absorption peaks were observed, indicating that the structure of components remained intactly during the preparation process, which was consistent with the XRD results. The intensity of SCN characteristic peaks in BOC/SCN was increased with the increment of SCN amounts, proving that the successful construction of heterojunction. Moreover, since the interaction between BOC and SCN altered the Bi-O bond, it could be found a slight blue shift at 539 cm^{-1} [38].

XPS was implemented to explore the chemical states and elemental composition of SCN, BOC, and BOC/SCN-3. As shown in the survey spectra (Fig. 4a), all peaks of C, N, O, Bi elements were easily detected in BOC/SCN-3 but without the S peak due to the low doping level of S in samples, which also was less prominent in SCN as suggested by the XRD and FTIR results. In order to further prove the existence of S, its chemical state was confirmed by the S 2p high resolution XPS spectra of BOC/SCN-3 (Fig. 4b). There was one S 2p peak at binding energy of 164.3 eV, which was attributed to the C-S bond formed via substituting S with lattice N [42]. In the C 1s spectra (Fig. 4c), the peaks of SCN at 288.5, 288.2 and 286.0 eV could be ascribed to the C–O bond, C sp^2 of N-C=N and CH-N on the edges of triazine unit, respectively, and the peak at 284.8 eV was ascribed to the adventitious carbon [43], which was also detected in BOC and BOC/SCN-3. Except for the adventitious carbon peak, the peak of BOC at 289.1 eV was ascribed to the CO_3^{2-} (O=C-O) in BOC [44]. While for BOC/SCN-3, the peaks positioned at 289.0, 288.0, 286.4 eV were ascribed to the CO_3^{2-}, C sp^2 of N-C=N and CH-N, respectively. In the N 1s spectra (Fig. 4d), the peaks of SCN around 399.6 and 398.6 eV were assigned to the tertiary nitrogen in N-$(C)_3$ groups and N sp^2 of C=N-C. After coupling with BOC, the N 1s peaks for BOC/SCN-3 shifted to higher binding energies (399.9 and 398.7 eV), which was probably due to the interaction between C atoms of CO_3^{2-} and N atoms [38]. The O 1s spectra (Fig. 4e) displayed three peaks at 532.1, 531.1 and 530.1 eV, corresponding to the adsorbed H_2O, carbonate ions (C-O) and Bi-O bond, respectively [26], and the distinct blue shift of binding energies was found in BOC/SCN-3. In the Bi 4f region (Fig. 4f), the spectra could be split into two peaks at 164.6 and 159.3 eV due to the Bi $4f_{5/2}$ and Bi $4f_{7/2}$ of Bi^{3+} [45, 46]. Interestingly, the Bi 4f spectra of BOC/SCN-3 showed the same shift tendency as the O 1s spectra, the reason would be that Bi and O atoms which obtained electrons increased the electron densities and thus possessed lower binding energies than pristine materials [47]. From the XPS analysis results above, the SCN and BOC were co-existed in the composite and the excellent electronic interactions were developed between them. In addition, the shift of characteristic peaks was caused by the formation of the 2D/1D heterojunction, which was beneficial for the electrons transfer.

3.3. Optical and electrochemical analysis

To investigate the optical response and band gap energy of the obtained samples, UV–vis diffuse reflectance spectra and valence band-XPS spectra were carried out.

As shown in Fig. 5a, the absorption edge of CN exhibited obvious red-shift in the visible range after doping with S (from 463 to 485 nm), confirming that S doping and tubular structure with multiple reflections of incident light enhanced the visible-light harvesting and produced more light-excited charge pairs. BOC presented a sheer absorption edge in the UV region but possessed the weakest visible-light absorption among all samples. And after coupling with SCN, the spectra of BOC/SCN were significantly shifted toward longer wavelength direction, and the absorbance intensity was increased with a wider absorption tail. In addition, with the increase of SCN dosage, the absorption range of composites gradually broadened, which was inconsistent with our expectations, suggesting that the photocatalytic activity was not only affected by the light absorption capacity. The band gaps (E_g) of CN and SCN were calculated to be about 2.55 eV and 2.24 eV by the Kubelka-Munk method (Fig. 5b), respectively. The doping of S atoms into the triazine units of CN formed weak covalent bonds with the adjacent N atoms, thereby narrowing the electronic band structure of SCN, which was in agreement with the literature reports [40]. With the collaborative interaction, the E_g of BOC/SCN-3 became narrower than pure BOC (3.20 eV), reaching approximately 2.12 eV. Meanwhile, the valence band (VB)-XPS spectra of SCN and BOC were measured in Fig. 5c. By linearly extrapolating the leading edge of VB to its intersection with the background count [48, 49], the VB edge potentials of SCN and BOC were determined at 1.24 eV and 3.41 eV. Based on the values of E_g, their corresponding conduction band (CB) positions were calculated to be -1.00 eV and 0.21 eV, respectively. In addition, the Mott-Schottky plots were also measured. As shown in Fig. S2, both SCN and BOC assigned to the n-type semiconductors owing to the positive slope and their flat band potentials (E_{fb}) were approximately -1.27 eV and -0.05 eV vs saturated calomel electrode (SCE), respectively, which were equivalent to -1.03 eV and 0.19 eV vs normal hydrogen electrode (NHE, $E_{NHE} = E_{SCE} + 0.24$ eV) [50]. The CB was generally considered to be equal to E_{fb} for n-type semiconductor [51-53], therefore the CB of SCN and BOC were -1.03 eV and 0.19 eV, which were close to the results obtained from the VB-XPS spectra, further confirming the accuracy of the band positions.

The PL spectrum was used to investigate the excitation and recombination efficiency of the photo-generated electron-hole pairs. From Fig. 5d, it was obvious that pristine BOC exhibited a strong PL emission intensity centering at approximately 460 nm under the excitation wavelength of 320 nm, which was attributed to the wide energy band gap (3.20 eV) and the direct recombination of photo-induced electrons and holes. Compared to BOC, the composite BOC/SCN-3 showed dramatic decrease in PL signals, indicating that the formed heterojunction effectively hindered the recombination and facilitated the transfer of charges, it was conducive to the degradation of TCH.

The above results were also verified by electrochemical measurements. As expected, the photocurrent response density of all samples reached steady-state under the light irradiation and the values dropped rapidly when the light was turned off (Fig. 5e), which was ascribed to the intrinsic photoresponse of semiconductor [54, 55]. In contrast to both BOC and SCN component, the BOC/SCN-3 heterojunction presented the highest photocurrent intensity, manifesting that the optimal separation rate of carriers was existed in composite. EIS was another important indicator for investigating the charge transfer dynamic. According to the Nyquist plots in Fig. 5f, the sequence of arc radii of three electrodes was BOC > SCN > BOC/SCN-3. This confirmed that BOC/SCN-3 had the lowest charge transfer resistance, thus speeding up the interfacial charge separation. Based on these characterization results, the excellent optical and electrochemical properties of BOC/SCN-3 were derived from the interaction between BOC and SCN through the 2D/1D heterostructure. The intimate contact in two components promoted the charge migration from single phase to composite phase and elevated spatial separation efficiency of electron-hole pairs at material interface.

3.4. Photocatalytic activity

3.4.1. Photocatalytic degradation of TCH

The photocatalytic performance of the synthesized catalysts was assessed towards TCH degradation under visible light irradiation, and the prepared solutions were stirred in the dark for 30 min to achieve adsorption-desorption equilibrium before the irradiation reaction. As shown in Fig. 6a, only 23.9% TCH was eliminated by CN within 30 min, while SCN exhibited 59.0% TCH degradation under the identical conditions, implying that the tubular structure formed by S doping effectively enhanced the photocatalytic activity of CN. In fact, the work function (WF) of CN was changed after S doping. Fig. S3 exhibited the UPS spectra of CN and SCN at an excitation energy (hν) of 21.20 eV. The secondary electron cutoff (SEC) of

CN was 17.21 eV, and that of SCN was 18.04 eV. Hence, the calculated work functions of CN and SCN were 3.99 eV and 3.16 eV, respectively (WF = hν - SEC) [56]. The lower work function indicated that the photogenerated electrons of semiconductor had a stronger escape ability [57], resulting in SCN had higher photocatalytic activity than CN. All composites showed superior adsorption capacities for TCH than bare BOC, which could be due to the increase in surface area provided more active sites. The degradation efficiency of composites was significantly enhanced and BOC/SCN-3 displayed the optimal degradation performance (82.6%) compared with BOC (38.2%). The increased photocatalytic activity was due to the enlarged light response range, well-matched band structure and rapid separation of electron-hole pairs caused by the construction of heterostructure. It was worth emphasizing that when the mass ratios of SCN to BOC gradually declined, the degradation trend of composites emerged a climb and then fell. Low content of SCN had negative effect on improving the photoresponse ability of BOC and promoting interface charge transfer, while excessive SCN could inhibit the crystal growth of BOC. In addition, compared with the pseudo-first-order kinetic model, the pseudo-second-order kinetic model produced a better fit to the degradation process (Fig. S4), and BOC/SCN-3 held the largest rate constant (0.01525 min^{-1}), which further proved that BOC/SCN-3 was an outstanding photocatalyst.

In order to further evaluate the complete removal efficiency for TCH of photocatalysts, the mineralization capacity was tested by TOC. Fig. 6b integrated the mineralization efficiency and photodegradation efficiency of BOC, SCN and

BOC/SCN-3. It could be seen that the mineralization efficiency was inferior to the corresponding photodegradation ones within 30 min irradiation time. In detail, the BOC/SCN-3 hybrid performed the 46.9% TOC removal in TCH aqueous solution, which was 2.2 and 1.5 times than that of BOC (21.3%) and SCN (30.1%), indicating that the hybrid had more effective degradation ability and more organic molecules were mineralized during the degradation process.

The reusability of photocatalyst was also a crucial index for the actual photocatalytic applications. To investigate the stability of BOC/SCN-3, it was checked in five sequential cycles of TCH photodegradation and the sample was filtered, washed and then dried after each cycling reaction. From the consequence of repeated experiments (Fig. 6c), the TCH degradation ratio still remained at 74.5% (fresh 82.6%) after five cycling runs, implying that BOC/SCN-3 heterojunction effectively avoided photocorrosion during the reaction and possessed long-term stability. The slight damage of photocatalytic activity might be owing to the inevitable mass loss of catalyst during each cycle test. In addition, the morphology and crystalline structure of BOC/SCN-3 after photocatalytic reaction were characterized. As shown in Fig. S5, the SEM and TEM images revealed that the morphology of BOC/SCN-3 remained unchanged after five times recycle experiments, and BOC still kept strong interfacial contact with SCN. The intensity of partial peaks in the XRD pattern after the reaction was slightly decreased than that before the reaction, which might be due to the mechanical damage caused by repeated washing. These results further proved the excellent reusability and photostability of the as-prepared

BOC/SCN-3.

3.4.2. Effect of initial TCH concentrations

In actual wastewater, the concentration of pollutants varied extensively and the effect of initial TCH concentrations on photocatalytic activity of photocatalyst should be discussed. Therefore, the degradation experiments with different TCH concentrations (5-30 mg L^{-1}) over BOC/SCN-3 sample were performed and the results were shown in Fig. 6d. The degradation efficiencies were 84.7% and 82.6% at the initial TCH concentrations equaled to 5 and 10 mg L^{-1}. With the TCH concentrations further increased to 15, 20 and 30 mg L^{-1}, the corresponding degradation efficiencies were greatly reduced to 70.1%, 57.1% and 50.3%, respectively, illustrating that the high initial TCH concentrations had perceptible negative effect on the photodegradation process, and BOC/SCN-3 was more suitable for treating low-concentration TCH wastewater. This phenomenon could be explained by the visible light transmittance and the intermediates accumulation. Specifically, high concentration of pollutants inevitably caused low light penetration, and the less photon inhibited the excitation of charges on the catalyst. Besides, the increased intermediates generated during the reaction intensified the adsorption competition on the surface of catalyst with parent TCH molecules and thereby leading to the hindrance of TCH degradation.

3.4.3. Effect of inorganic anions

Normally, the removed target pollutants coexisted with common inorganic anions in actual wastewater, which would interfere with the photocatalytic activity.

Therefore, the effect of inorganic anions (CO_3^{2-}, Cl^-, SO_4^{2-}) on the degradation process was simulated by BOC/SCN-3 catalyst and relevant sodium salts (0.05 M) were employed in order to avoid the influence of extra cations. It could be seen from the Fig. 6e that these three anions had different degrees of impact on the degradation efficiency. The presence of CO_3^{2-} promoted the adsorption and final degradation efficiency of TCH, which could be ascribed to the HCO_3^{2-} and OH^- generated by the hydrolysis of CO_3^{2-} increased the alkalinity of the solution [31]. A significantly inhibition effect on TCH degradation was found within Cl^- and SO_4^{2-} electrolytes due to the competitive adsorption between ions and antibiotic molecules. In addition, SO_4^{2-} could act radical scavengers for •OH and h^+ [58], the limited number of radicals accounted for the largest negative effect on TCH degradation of SO_4^{2-}.

3.4.4. Effect of reaction pH

It was well-known that TCH existed as three forms (TCH^+, TCH^0 and TCH^-) under different pH conditions (pH < 4, 4 < pH < 7.5 and pH > 7.5) [59, 60]. The reaction pH would affect the production of reactive oxygen species and then change the degradation activity of pollutants. In this study, the pH value of pristine TCH solution was 4.86, and other pH of the reaction system was adjusted by NaOH (0.1 M) or HNO_3 (0.1 M). The Zeta potentials of BOC/SCN-3 gradually decreased as pH increases and turned from positive to negative when the pH was around 7.6 (Fig. S6).

According to the degradation curves of TCH over BOC/SCN-3 in different pH solutions (Fig. 6f), the adsorption capacity and degradation efficiency decreased visibly under strong acid conditions (pH = 3), which was ascribed to the increased repulsive force between the TCH^+ and the catalyst with positively charges. Under alkaline conditions, the catalyst exhibited superior adsorption capacity, implying that the surface complexation was more intensive than the repulsive force and played a leading role in absorbing TCH [61]. However, the degradation efficiency significantly decreased from 86.6% to 74.4% when the pH regulated from 9 to 11, it might be because excessive antibiotic adsorption suppressed the utilization of photons. Besides, redundant OH^- could consume partial •OH and h^+ [62], which was also responsible for the restrained photocatalytic performance. The above results indicated that the weak acid or weak alkali conditions were more favorable for the TCH photodegradation.

3.5. Photocatalytic mechanism

The reactive radicals would generate in the reaction system and be expected to play crucial roles in the photocatalytic process. In order to clarify the reaction mechanism, the reactive radicals trapping experiments over BOC/SCN-3 catalyst were carried out by adding sacrificial agents, in which disodium edetate (EDTA-2Na), 4-hydroxy-TEMPO (HTEMPO) and isopropanol (IPA) acted as h^+, $•O_2^-$ and •OH scavengers, respectively. As shown in Fig. 7a, the degradation efficiency of TCH was most reduced after the addition of EDTA-2Na among the four control groups, suggesting that h^+ was the predominant active species for TCH degradation. It could be observed a slight decrease in the photocatalytic activity by the introduction of HTEMPO, indicating that $•O_2^-$ was also involved in the reaction process. However, an ignorable trapping effect was exhibited by IPA, which meant that the hybrid hardly produced •OH. Hence, it could be preliminarily considered that h^+ and $•O_2^-$ both contributed to the TCH degradation and the former played a major role.

To further verify whether h^+, $•O_2^-$ and •OH existed in the photocatalytic system, the ESR technology with TEMPO and DMPO spin-trapping was employed in acetonitrile solution and methanol solution, respectively. Fig. 7b displayed the ESR signals of TEMPO-h^+ at dark and irradiation conditions. A triplet ESR signal could be visibly observed in dark, which was derived from the signal generated by TEMPO itself [63]. The TEMPO would react with h^+ to generate the spin-adduct and then decrease the signal intensity of ESR, namely, the weakened signal of TEMPO-h^+ indicated the generation of h^+ [64]. Compared to the dark condition, the all ESR signals of TEMPO-h^+ were reduced after 10 min light irradiation, and the composite exhibited the lowest signal strength among the three materials, indicating that BOC/SCN-3 had the optimal electron-hole pairs separation efficiency and more h^+ was generated. Different from TEMPO, DMPO could not produce ESR signal by itself, it would form ESR signal after reacting with active species [65]. As shown in Fig. 7c, no obvious DMPO-$•O_2^-$ signal of individual BOC was found, which attributed to its CB potential (0.21 eV vs NHE) was more positive than the $O_2/•O_2^-$ potentials (−0.33 eV vs NHE) [66]. Remarkably, the signal intensity of SCN was stronger than that of BOC/SCN-3, the decrease of $•O_2^-$ might be due to the more singlet oxygen was produced by BOC/SCN-3 during the molecular oxygen activation [67]. Meanwhile, four characteristic peaks of DMPO-•OH for SCN and BOC were probed in Fig. 7d, based on their VB potentials, the generation of •OH for SCN was derived from the reduction of $•O_2^−$ [68]. However, there was no obvious DMPO-•OH signal for BOC/SCN-3, which was probably because the h^+ reacted directly with pollutants instead of oxidizing H_2O or $OH^−$ to generate •OH [69]. These results proved that both h^+ and $•O_2^−$ were involved in the BOC/SCN-3 reaction system, which were corroborated the conclusion of the reactive radicals trapping experiments.

Therefore, combined with the previous analysis, the possible mechanism for TCH degradation at the interface of BOC/SCN heterojunction was put forward. The suitable overlapping band structure of SCN (CB = −1.00 eV, VB = 1.24 eV vs NHE) and BOC (CB = 0.21 eV, VB = 3.41 eV vs NHE) could construct an effective heterojunction. For the traditional type II heterojunction, the photo-excited electrons would accumulate in the CB of BOC, whose potential was positive than the $O_2/•O_2^−$ potential and the electrons could not reduce the dissolved O_2 to $•O_2^−$ [63]. Meanwhile, most photo-generated holes would be located in the VB of SCN, the weak oxidizing ability was contrary to the decisive role of holes in the degradation process. In fact, according to the XPS results, the N 1s spectra and the Bi 4f spectra of BOC/SCN-3 respectively shifted positively and negatively compared with that of SCN and BOC component, manifesting that SCN surface possessed positive charges and BOC surface possessed negative charges, and thus a built-in electric field was created at the heterojunction interface [70]. In view of this, the photo-excited electrons would transfer from the CB of BOC to the VB of SCN through the driving force of interfacial electronic interaction. As a result, the Z-scheme charge migration system was more in line with expectation of photocatalytic mechanism (Fig. 8). After being excited by the visible light, the electrons transferred from the CB of BOC quickly recombined with the holes in the VB of SCN. Hence, the electrons generated from SCN were mainly concentrated in the CB of SCN, and they effectively reduced the dissolved O_2 to $\bullet O_2^-$ to degrade TCH. The holes generated from BOC were still stored in the VB and directly participated in the reaction. The impressive reducibility and oxidizability of Z-scheme heterojunction could degrade TCH into H_2O, CO_2 and other small molecules with high efficiency. The major possible reactions were described as follows:

$$\mathrm{BOC} + h\nu \rightarrow e_{CB}^-\ (\mathrm{BOC}) + h_{VB}^+\ (\mathrm{BOC}) \tag{1}$$

$$\mathrm{SCN} + h\nu \rightarrow e_{CB}^-\ (\mathrm{SCN}) + h_{VB}^+\ (\mathrm{SCN}) \tag{2}$$

$$e_{CB}^-\ (\mathrm{BOC}) + h_{VB}^+\ (\mathrm{SCN}) \rightarrow \text{recombination} \tag{3}$$

$$e_{CB}^-\ (\mathrm{SCN}) + O_2 \rightarrow \bullet O_2^- \tag{4}$$

$$h_{VB}^+\ (\mathrm{BOC}) + \bullet O_2^- + \mathrm{TCH} \rightarrow \text{products} \tag{5}$$

In summary, the enhanced photocatalytic activity of BOC/SCN binary photocatalytic system was owing to the following aspects. Firstly, the morphology, bandgap and work function of CN were regulated by S doping, and SCN boosted the visible light harvesting and electrons escape ability. Secondly, BOC was grown in situ on SCN surface, the intimate contact and strong binding strength between them accelerated the migration of photo-induced carriers. Furthermore, the 2D/1D Z-scheme heterojunction formed by the well-matched energy level promoted electrons to travel along the 1D longitudinal and radial directions, so that the recombination of charges was restrained sufficiently. Last but not least, the enlarged BET surface area was favorable for pollutants adsorption and intermediates diffusion. The synergistic effect of these aspects forcefully explained the excellent photocatalytic performance of BOC/SCN catalyst.

4. Conclusion

Herein, a novel visible-light responsive 2D/1D $Bi_2O_2CO_3$ nanoflake/S-doped g-C_3N_4 hollow tube hierarchical heterostructure was constructed by in situ hydrothermal method. The BOC nanoflakes grew parallel on the surface of SCN and possessed strong interfacial contact with SCN. The binary photocatalytic system exhibited 82.6% TCH degradation efficiency within 30 min irradiation, which was 2.2 and 3.5 times higher than pristine BOC and CN. Both S doping and the hierarchical heterostructure were crucial reasons for the improvement of photocatalytic performance. Based on various characterization techniques, the BOC/SCN-3 was found to possess outstanding morphology, optical and electrochemical properties. Mechanism analysis revealed that due to the well-matched energy level and built-in electric field, the formed Z-scheme structure extremely promoted the transfer of interface charges and achieved the spatial separation of electron-hole pairs. This work pointed out a new route to develop Z-scheme heterojunction photocatalyst with unique structure for efficient antibiotic degradation.

Acknowledgements

The study was financially supported by the Program for Changjiang Scholars and Innovative Research Team in University (IRT-13R17), the National Natural Science Foundation of China (51979103, 51909085, 51679085, 51579096, 51521006, 51508177), the Fundamental Research Funds for the Central Universities of China (531107051205), the Funds of Hunan Science and Technology Innovation Project (2018RS3115, 2020RC5012), the Key Research and Development Project of Hunan Province of China (2017SK2241).

References:

[1] A. Karkman, K. Parnanen, D.G.J. Larsson, Fecal pollution can explain antibiotic resistance gene abundances in anthropogenically impacted environments, Nat. Commun. 10 (2019) 80.
[2] C. Dhand, M. Venkatesh, V.A. Barathi, S. Harini, S. Bairagi, E.G.T. Leng, N. Muruganandham, K.Z.W. Low, M. Fazil, X.J. Loh, D.K. Srinivasan, S.P. Liu, R.W. Beuerman, N.K. Verma, S. Ramakrishna, R. Lakshminarayanan, Bio-inspired crosslinking and matrix-drug interactions for advanced wound dressings with long-term antimicrobial activity, Biomaterials 138 (2017) 153-168.
[3] M.B. Ahmed, J.L. Zhou, H.H. Ngo, W.S. Guo, Adsorptive removal of antibiotics from water and wastewater: Progress and challenges, Sci. Total Environ. 532 (2015) 112-126.
[4] S. Rodriguez-Mozaz, S. Chamorro, E. Marti, B. Huerta, M. Gros, A. Sanchez-Melsio, C.M. Borrego, D. Barcelo, J.L. Balcazar, Occurrence of antibiotics and antibiotic resistance genes in hospital and urban wastewaters and their impact on the receiving river, Water Res. 69 (2015) 234-242.
[5] B.B. Shao, Z.F. Liu, G.M. Zeng, Y. Liu, X. Yang, C.Y. Zhou, M. Chen, Y.J. Liu, Y.L. Jiang, M. Yan, Immobilization of laccase on hollow mesoporous carbon nanospheres: noteworthy immobilization, excellent stability and efficacious for antibiotic contaminants removal, J. Hazard. Mater. 362 (2019) 318-326.
[6] H. Wang, Y. Wu, M. Feng, W. Tu, T. Xiao, T. Xiong, H. Ang, X. Yuan, J.W. Chew, Visible-light-driven removal of tetracycline antibiotics and reclamation of

hydrogen energy from natural water matrices and wastewater by polymeric carbon nitride foam, Water Res. 144 (2018) 215-225.

[7] Y. Lou, Z.-L. Ye, S. Chen, Q. Wei, J. Zhang, X. Ye, Influences of dissolved organic matters on tetracyclines transport in the process of struvite recovery from swine wastewater, Water Res. 134 (2018) 311-326.

[8] T. Wu, X.J. Liu, Y. Liu, M. Cheng, Z.F. Liu, G.M. Zeng, B.B. Shao, Q.H. Liang, W. Zhang, Q.Y. He, W. Zhang, Application of QD-MOF composites for photocatalysis: energy production and environmental remediation, Coord. Chem. Rev. 403 (2020) 213097.

[9] Y. Pan, X. Liu, W. Zhang, Z. Liu, G. Zeng, B. Shao, Q. Liang, Q. He, X. Yuan, D. Huang, M. Chen, Advances in photocatalysis based on fullerene C_{60} and its derivatives: properties, mechanism, synthesis, and applications, Appl. Catal. B-Environ. 265 (2020) 118579.

[10] Y. Liu, Z.F. Liu, D.L. Huang, M. Cheng, G.M. Zeng, C. Lai, C. Zhang, C.Y. Zhou, W.J. Wang, D.N. Jiang, H. Wang, B.B. Shao, Metal or metal-containing nanoparticle@MOF nanocomposites as a promising type of photocatalyst, Coord. Chem. Rev. 388 (2019) 63-78.

[11] B. Shao, Z. Liu, G. Zeng, Y. Liu, Q. Liang, Q. He, T. Wu, Y. Pan, J. Huang, Z. Peng, S. Luo, C. Liang, X. Liu, S. Tong, J. Liang, Synthesis of 2D/2D CoAl-LDHs/$Ti_3C_2T_x$ Schottky-junction with enhanced interfacial charge transfer and visible-light photocatalytic performance, Appl. Catal. B-Environ. 286 (2021) 119867.

[12] C. Feng, L. Tang, Y. Deng, J. Wang, Y. Liu, X. Ouyang, Z. Chen, H. Yang, J. Yu, J. Wang, Maintaining stable LSPR performance of $W_{18}O_{49}$ by protecting its oxygen vacancy: A novel strategy for achieving durable sunlight driven photocatalysis, Appl. Catal. B-Environ. 276 (2020) 119167.

[13] R.B. Li, M.X. Cai, Z.J. Xie, Q.X. Zhang, Y.Q. Zeng, H.J. Liu, G.G. Liu, W.Y. Lv, Construction of heterostructured $CuFe_2O_4$/g-C_3N_4 nanocomposite as an efficient visible light photocatalyst with peroxydisulfate for the organic oxidation, Appl. Catal. B-Environ. 244 (2019) 974-982.

[14] D. Zhang, X. Liu, S. Wang, B. Fan, Z. Shao, C. Su, X. Pu, Enhanced charges separation to improve hydrogen production efficiency by organic piezoelectric film polarization, J. Alloy. Compd. 869 (2021) 159390.

[15] B. Shao, Z. Liu, G. Zeng, H. Wang, Q. Liang, Q. He, M. Cheng, C. Zhou, L. Jiang, B. Song, Two-dimensional transition metal carbide and nitride (MXene) derived quantum dots (QDs): synthesis, properties, applications and prospects, J. Mater. Chem. A 8 (2020) 7508-7535.

[16] Y. Lu, Y. Li, Y. Wang, J. Zhang, Two-photon induced NIR active core-shell structured WO_3/CdS for enhanced solar light photocatalytic performance, Appl. Catal. B-Environ. 272 (2020) 118979.

[17] B.B. Shao, Z.F. Liu, G.M. Zeng, Z.B. Wu, Y. Liu, M. Cheng, M. Chen, Y.J. Liu, W. Zhang, H.P. Feng, Nitrogen-doped hollow mesoporous carbon spheres modified g-C_3N_4/Bi_2O_3 direct dual semiconductor photocatalytic system with enhanced antibiotics degradation under visible light, ACS Sustain. Chem. Eng. 6 (2018) 16424-16436.

[18] P. Chen, H. Liu, Y. Sun, J. Li, W. Cui, L.a. Wang, W. Zhang, X. Yuan, Z. Wang, Y. Zhang, F. Dong, Bi metal prevents the deactivation of oxygen vacancies in $Bi_2O_2CO_3$ for stable and efficient photocatalytic NO abatement, Appl. Catal. B-Environ. 264 (2020) 118545.

[19] Y. Huang, D.D. Zhu, Q. Zhang, Y.F. Zhang, J.J. Cao, Z.X. Shen, W.K. Ho, S.C. Lee, Synthesis of a $Bi_2O_2CO_3/ZnFe_2O_4$ heterojunction with enhanced photocatalytic activity for visible light irradiation-induced NO removal, Appl. Catal. B-Environ. 234 (2018) 70-78.

[20] D. Majhi, K. Das, A. Mishra, R. Dhiman, B.G. Mishra, One pot synthesis of $CdS/BiOBr/Bi_2O_2CO_3$: A novel ternary double Z-scheme heterostructure photocatalyst for efficient degradation of atrazine, Appl. Catal. B-Environ. 260 (2020) 118222.

[21] Z.F. Liu, Y.L. Jiang, X.J. Liu, G.M. Zeng, B.B. Shao, Y.J. Liu, Y. Liu, W. Zhang, W. Zhang, M. Yan, X. He, Silver chromate modified sulfur doped graphitic carbon nitride microrod composites with enhanced visible-light photoactivity towards organic pollutants degradation, Compos. Pt. B-Eng. 173 (2019) 106918.

[22] R. Rameshbabu, P. Ravi, M. Sathish, Cauliflower-like CuS/ZnS nanocomposites decorated g-C_3N_4 nanosheets as noble metal-free photocatalyst for superior photocatalytic water splitting, Chem. Eng. J. 360 (2019) 1277-1286.

[23] S. Ali, M. Humayun, W. Pi, Y. Yuan, M. Wang, A. Khan, P. Yue, L. Shu, Z. Zheng, Q. Fu, W. Luo, Fabrication of $BiFeO_3$-g-C_3N_4-WO_3 Z-scheme heterojunction as highly efficient visible-light photocatalyst for water reduction and 2,4-dichlorophenol degradation: Insight mechanism, J. Hazard. Mater. 397 (2020) 122708.

[24] Y.J. Ma, Y. Bian, P.F. Tan, Y.Y. Shang, Y. Liu, L.D. Wu, A.Q. Zhu, W.W. Liu, X. Xiong, J. Pan, Simple and facile ultrasound-assisted fabrication of $Bi_2O_2CO_3$/g-C_3N_4 composites with excellent photoactivity, J. Colloid Interface Sci. 497 (2017) 144-154.

[25] Z. Wang, Y. Huang, W. Ho, J. Cao, Z. Shen, S.C. Lee, Fabrication of $Bi_2O_2CO_3$/g-C_3N_4 heterojunctions for efficiently photocatalytic NO in air removal: In-situ self-sacrificial synthesis, characterizations and mechanistic study, Appl. Catal. B-Environ. 199 (2016) 123-133.

[26] Y. Lan, Z. Li, W. Xie, D. Li, G. Yan, S. Guo, C. Pan, J. Wu, In situ fabrication of I-doped $Bi_2O_2CO_3$/g-C_3N_4 heterojunctions for enhanced photodegradation activity under visible light, J. Hazard. Mater. 385 (2020) 121622.

[27] J. Li, X.Y. Wu, Z. Wan, H. Chen, G.K. Zhang, Full spectrum light driven photocatalytic in-situ epitaxy of one-unit-cell $Bi_2O_2CO_3$ layers on Bi_2O_4 nanocrystals for highly efficient photocatalysis and mechanism unveiling, Appl. Catal. B-Environ. 243 (2019) 667-677.

[28] Q. Liang, B. Shao, S. Tong, Z. Liu, L. Tang, Y. Liu, M. Cheng, Q. He, T. Wu, Y. Pan, J. Huang, Z. Peng, Recent advances of melamine self-assembled graphitic carbon nitride-based materials: Design, synthesis and application in energy and environment, Chem. Eng. J. 405 (2021) 126951.

[29] X. Li, J. Zhang, Y. Huo, K. Dai, S. Li, S. Chen, Two-dimensional sulfur- and

chlorine-codoped g-C_3N_4/CdSe-amine heterostructures nanocomposite with effective interfacial charge transfer and mechanism insight, Appl. Catal. B-Environ. 280 (2021) 119452.

[30] L. Chen, D. Zhu, J. Li, X. Wang, J. Zhu, P.S. Francis, Y. Zheng, Sulfur and potassium co-doped graphitic carbon nitride for highly enhanced photocatalytic hydrogen evolution, Appl. Catal. B-Environ. 273 (2020) 119050.

[31] Q. Liang, X. Liu, J. Wang, Y. Liu, Z. Liu, L. Tang, B. Shao, W. Zhang, S. Gong, M. Cheng, Q. He, C. Feng, In-situ self-assembly construction of hollow tubular g-C_3N_4 isotype heterojunction for enhanced visible-light photocatalysis: experiments and theories, J. Hazard. Mater. (2020) 123355.

[32] H. Hou, X. Zhang, Rational design of 1D/2D heterostructured photocatalyst for energy and environmental applications, Chem. Eng. J. 395 (2020) 125030.

[33] R.P. Hu, X. Xiao, S.H. Tu, X.X. Zuo, J.M. Nan, Synthesis of flower-like heterostructured beta-Bi_2O_3/$Bi_2O_2CO_3$ microspheres using $Bi_2O_2CO_3$ self-sacrifice precursor and its visible-light-induced photocatalytic degradation of o-phenylphenol, Appl. Catal. B-Environ. 163 (2015) 510-519.

[34] B. Shao, X. Liu, Z. Liu, G. Zeng, W. Zhang, Q. Liang, Y. Liu, Q. He, X. Yuan, D. Wang, S. Luo, S. Gong, Synthesis and characterization of 2D/0D g-C_3N_4/CdS-nitrogen doped hollow carbon spheres (NHCs) composites with enhanced visible light photodegradation activity for antibiotic, Chem. Eng. J. 374 (2019) 479-493.

[35] M. Wu, J. Zhang, B.-b. He, H.-w. Wang, R. Wang, Y.-s. Gong, In-situ construction of coral-like porous P-doped g-C_3N_4 tubes with hybrid 1D/2D architecture and high efficient photocatalytic hydrogen evolution, Appl. Catal. B-Environ. 241 (2019) 159-166.

[36] W. Wang, Q. Niu, G. Zeng, C. Zhang, D. Huang, B. Shao, C. Zhou, Y. Yang, Y. Liu, H. Guo, W. Xiong, L. Lei, S. Liu, H. Yi, S. Chen, X. Tang, 1D porous tubular g-C_3N_4 capture black phosphorus quantum dots as 1D/0D metal-free photocatalysts for oxytetracycline hydrochloride degradation and hexavalent chromium reduction, Appl. Catal. B-Environ. 273 (2020) 119051.

[37] P. Ding, J. Di, X. Chen, J. Zhao, K. Gu, Y. Zhang, S. Yin, G. Liu, J. Xia, H. Li, Partially etched $Bi_2O_2CO_3$ by metal chloride for enhanced reactive oxygen species generation: A tale of two strategies, Appl. Catal. B-Environ. 245 (2019) 325-333.

[38] H.P. Zhao, G.F. Li, F. Tian, Q.T. Jia, Y.L. Liu, R. Chen, g-C_3N_4 surface-decorated $Bi_2O_2CO_3$ for improved photocatalytic performance: Theoretical calculation and photodegradation of antibiotics in actual water matrix, Chem. Eng. J. 366 (2019) 468-479.

[39] S. Zhang, Y. Liu, P. Gu, R. Ma, T. Wen, G. Zhao, L. Li, Y. Ai, C. Hu, X. Wang, Enhanced photodegradation of toxic organic pollutants using dual-oxygen-doped porous g-C_3N_4: Mechanism exploration from both experimental and DFT studies, Appl. Catal. B-Environ. 248 (2019) 1-10.

[40] D.P. Sahoo, K.K. Das, S. Patnaik, K. Parida, Double charge carrier mechanism through 2D/2D interface-assisted ultrafast water reduction and antibiotic degradation over architectural S,P co-doped g-C_3N_4/ZnCr LDH photocatalyst, Inorg. Chem. Front.

7 (2020) 3695-3717.

[41] W. Zhang, Y. Sun, F. Dong, W. Zhang, S. Duan, Q. Zhang, Facile synthesis of organic–inorganic layered nanojunctions of g-C_3N_4/$(BiO)_2CO_3$ as efficient visible light photocatalyst, Dalton Trans. 43 (2014) 12026-12036.

[42] G. Liu, P. Niu, C. Sun, S.C. Smith, Z. Chen, G.Q. Lu, H.-M. Cheng, Unique electronic structure induced high photoreactivity of sulfur-doped graphitic C_3N_4, J. Am. Chem. Soc. 132 (2010) 11642-11648.

[43] Y. Yang, Z. Zeng, G. Zeng, D. Huang, R. Xiao, C. Zhang, C. Zhou, W. Xiong, W. Wang, M. Cheng, W. Xue, H. Guo, X. Tang, D. He, Ti_3C_2 Mxene/porous g-C_3N_4 interfacial Schottky junction for boosting spatial charge separation in photocatalytic H_2O_2 production, Appl. Catal. B-Environ. 258 (2019) 117956.

[44] M. Sun, S.L. Li, T. Yan, P.G. Ji, X. Zhao, K. Yuan, D. Wei, B. Du, Fabrication of heterostructured $Bi_2O_2CO_3$/Bi_2O_4 photocatalyst and efficient photodegradation of organic contaminants under visible-light, J. Hazard. Mater. 333 (2017) 169-178.

[45] L.H. Yu, X.Y. Zhang, G.W. Li, Y.T. Cao, Y. Shao, D.Z. Li, Highly efficient $Bi_2O_2CO_3$/BiOCl photocatalyst based on heterojunction with enhanced dye-sensitization under visible light, Appl. Catal. B-Environ. 187 (2016) 301-309.

[46] L. Chen, R. Huang, S.F. Yin, S.L. Luo, C.T. Au, Flower-like $Bi_2O_2CO_3$: Facile synthesis and their photocatalytic application in treatment of dye-containing wastewater, Chem. Eng. J. 193 (2012) 123-130.

[47] Z. Zhao, Y. Zhou, F. Wang, K. Zhang, S. Yu, K. Cao, Polyaniline-decorated {001} facets of $Bi_2O_2CO_3$ nanosheets: In situ oxygen vacancy formation and enhanced visible light photocatalytic activity, ACS Appl. Mater. Interfaces 7 (2015) 730-737.

[48] G.P. Zhang, D.Y. Chen, N.J. Li, Q.F. Xu, H. Li, J.H. He, J.M. Lu, Fabrication of Bi_2MoO_6/ZnO hierarchical heterostructures with enhanced visible-light photocatalytic activity, Appl. Catal. B-Environ. 250 (2019) 313-324.

[49] L.L. Zhang, C. Hu, H.H. Ji, p-AgI anchored on {001} facets of n-$Bi_2O_2CO_3$ sheets with enhanced photocatalytic activity and stability, Appl. Catal. B-Environ. 205 (2017) 34-41.

[50] Y.Y. Zhao, Y.B. Wang, X.H. Liang, H.X. Shi, C.J. Wang, J. Fan, X.Y. Hu, E.Z. Liu, Enhanced photocatalytic activity of Ag-$CsPbBr_3$/CN composite for broad spectrum photocatalytic degradation of cephalosporin antibiotics 7-ACA, Appl. Catal. B-Environ. 247 (2019) 57-69.

[51] J. Ding, Z. Dai, F. Qin, H.P. Zhao, S. Zhao, R. Chen, Z-scheme $BiO_{1-x}Br$/$Bi_2O_2CO_3$ photocatalyst with rich oxygen vacancy as electron mediator for highly efficient degradation of antibiotics, Appl. Catal. B-Environ. 205 (2017) 281-291.

[52] L. Tang, C.Y. Feng, Y.C. Deng, G.M. Zeng, J.J. Wang, Y.N. Liu, H.P. Peng, J.J. Wang, Enhanced photocatalytic activity of ternary Ag/g-C_3N_4/$NaTaO_3$ photocatalysts under wide spectrum light radiation: The high potential band protection mechanism, Appl. Catal. B-Environ. 230 (2018) 102-114.

[53] Z. Wang, M. Chen, Y. Huang, X. Shi, Y. Zhang, T. Huang, J. Cao, W. Ho, S.C. Lee, Self-assembly synthesis of boron-doped graphitic carbon nitride hollow tubes for

enhanced photocatalytic NOx removal under visible light, Appl. Catal. B-Environ. 239 (2018) 352-361.

[54] P. Ding, J. Di, X. Chen, M. Ji, K. Gu, S. Yin, G. Liu, F. Zhang, J. Xia, H. Li, S, N codoped graphene quantum dots embedded in $(BiO)_2CO_3$: Incorporating enzymatic-like catalysis in photocatalysis, ACS Sustain. Chem. Eng. 6 (2018) 10229-10240.

[55] B. Shao, J. Wang, Z. Liu, G. Zeng, L. Tang, Q. Liang, Q. He, T. Wu, Y. Liu, X. Yuan, Ti_3C_2Tx MXene decorated black phosphorus nanosheets with improved visible-light photocatalytic activity: experimental and theoretical studies, J. Mater. Chem. A 8 (2020) 5171-5185.

[56] Z. Fang, Q. Li, L. Su, J.H. Chen, K.C. Chou, X.M. Hou, Efficient synergy of photocatalysis and adsorption of hexavalent chromium and rhodamine B over Al_4SiC_4/rGO hybrid photocatalyst under visible-light irradiation, Appl. Catal. B-Environ. 241 (2019) 548-560.

[57] H. Jiang, Z. Xing, T. Zhao, Z. Yang, K. Wang, Z. Li, S. Yang, L. Xie, W. Zhou, Plasmon Ag nanoparticle/Bi_2S_3 ultrathin nanobelt/oxygen-doped flower-like MoS_2 nanosphere ternary heterojunctions for promoting charge separation and enhancing solar-driven photothermal and photocatalytic performances, Appl. Catal. B-Environ. 274 (2020) 118947.

[58] Y. Yang, Z. Zeng, C. Zhang, D. Huang, G. Zeng, R. Xiao, C. Lai, C. Zhou, H. Guo, W. Xue, M. Cheng, W. Wang, J. Wang, Construction of iodine vacancy-rich BiOI/Ag@AgI Z-scheme heterojunction photocatalysts for visible-light-driven tetracycline degradation: Transformation pathways and mechanism insight, Chem. Eng. J. 349 (2018) 808-821.

[59] F. Deng, L. Zhao, X. Luo, S. Luo, D.D. Dionysiou, Highly efficient visible-light photocatalytic performance of Ag/$AgIn_5S_8$ for degradation of tetracycline hydrochloride and treatment of real pharmaceutical industry wastewater, Chem. Eng. J. 333 (2018) 423-433.

[60] Y. Pan, X. Yuan, L. Jiang, H. Wang, H. Yu, J. Zhang, Stable self-assembly AgI/UiO-66(NH_2) heterojunction as efficient visible-light responsive photocatalyst for tetracycline degradation and mechanism insight, Chem. Eng. J. 384 (2020) 123310.

[61] T. Tang, Z. Yin, J. Chen, S. Zhang, W. Sheng, W. Wei, Y. Xiao, Q. Shi, S. Cao, Novel p-n heterojunction Bi_2O_3/Ti^{3+}-TiO_2 photocatalyst enables the complete removal of tetracyclines under visible light, Chem. Eng. J. (2020) 128058.

[62] M. Chen, C. Guo, S. Hou, J. Lv, Y. Zhang, H. Zhang, J. Xu, A novel Z-scheme AgBr/P-g-C_3N_4 heterojunction photocatalyst: Excellent photocatalytic performance and photocatalytic mechanism for ephedrine degradation, Appl. Catal. B-Environ. 266 (2020) 118614.

[63] G. Zhao, J. Ding, F. Zhou, X. Chen, L. Wei, Q. Gao, K. Wang, Q. Zhao, Construction of a visible-light-driven magnetic dual Z-scheme $BiVO_4$/g-C_3N_4/$NiFe_2O_4$ photocatalyst for effective removal of ofloxacin: Mechanisms and degradation pathway, Chem. Eng. J. 405 (2021) 126704.

[64] Y. Yang, G.M. Zeng, D.L. Huang, C. Zhang, D.H. He, C.Y. Zhou, W.J. Wang,

W.P. Xiong, B. Song, H. Yi, S.J. Ye, X.Y. Ren, In situ grown single-atom cobalt on polymeric carbon nitride with bidentate ligand for efficient photocatalytic degradation of refractory antibiotics, Small 16 (2020) 2001634.

[65] R. Xiao, C. Zhao, Z. Zou, Z. Chen, L. Tian, H. Xu, H. Tang, Q. Liu, Z. Lin, X. Yang, In situ fabrication of 1D CdS nanorod/2D Ti_3C_2 MXene nanosheet Schottky heterojunction toward enhanced photocatalytic hydrogen evolution, Appl. Catal. B-Environ. 268 (2020) 118382.

[66] B.B. Shao, X.J. Liu, Z. Liu, G.M. Zeng, Q.H. Liang, C. Liang, Y. Cheng, W. Zhang, Y. Liu, S.X. Gong, A novel double Z-scheme photocatalyst $Ag_3PO_4/Bi_2S_3/Bi_2O_3$ with enhanced visible-light photocatalytic performance for antibiotic degradation, Chem. Eng. J. 368 (2019) 730-745.

[67] Z. Wang, H. Wang, Z. Zeng, G. Zeng, P. Xu, R. Xiao, D. Huang, X. Chen, L. He, C. Zhou, Y. Yang, Z. Wang, W. Wang, W. Xiong, Metal-organic frameworks derived $Bi_2O_2CO_3$/porous carbon nitride: A nanosized Z-scheme systems with enhanced photocatalytic activity, Appl. Catal. B-Environ. 267 (2020) 118700.

[68] Y. Yang, C. Zhang, D.L. Huang, G.M. Zeng, J.H. Huang, C. Lai, C.Y. Zhou, W.J. Wang, H. Guo, W.J. Xue, R. Deng, M. Cheng, W.P. Xiong, Boron nitride quantum dots decorated ultrathin porous g-C_3N_4: Intensified exciton dissociation and charge transfer for promoting visible-light-driven molecular oxygen activation, Appl. Catal. B-Environ. 245 (2019) 87-99.

[69] T. Xiong, M. Wen, F. Dong, J. Yu, L. Han, B. Lei, Y. Zhang, X. Tang, Z. Zang, Three dimensional Z-scheme $(BiO)_2CO_3/MoS_2$ with enhanced visible light photocatalytic NO removal, Appl. Catal. B-Environ. 199 (2016) 87-95.

[70] Y. Wang, C. Zhu, G. Zuo, Y. Guo, W. Xiao, Y. Dai, J. Kong, X. Xu, Y. Zhou, A. Xie, C. Sun, Q. Xian, 0D/2D Co_3O_4/TiO_2 Z-Scheme heterojunction for boosted photocatalytic degradation and mechanism investigation, Appl. Catal. B-Environ. 278 (2020) 119298.

[71] W. Shan, Y. Hu, Z. Bai, M. Zheng, C. Wei, In situ preparation of g-C_3N_4/bismuth-based oxide nanocomposites with enhanced photocatalytic activity, Appl. Catal. B-Environ. 188 (2016) 1-12.

[72] M. Xiong, L. Chen, Q. Yuan, J. He, S.-L. Luo, C.-T. Au, S.-F. Yin, Facile fabrication and enhanced photosensitized degradation performance of the g-C_3N_4-$Bi_2O_2CO_3$ composite, Dalton Trans. 43 (2014) 8331-8337.

[73] Q.T. Zhanga, B. Xu, S.S. Yuan, M. Zhang, T. Ohno, Improving g-C_3N_4 photocatalytic performance by hybridizing with $Bi_2O_2CO_3$ nanosheets, Catal. Today 284 (2017) 27-36.

[74] N. Tian, H.W. Huang, Y.X. Guo, Y. He, Y.H. Zhang, A g-$C_3N_4/Bi_2O_2CO_3$ composite with high visible-light-driven photocatalytic activity for rhodamine B degradation, Appl. Surf. Sci. 322 (2014) 249-254.

[75] Y. Duan, H. Yao, J. Li, X. Shang, D. Jia, C. Li, A facile one-pot preparation of $Bi_2O_2CO_3$/g-C_3N_4 composites with enhanced photocatalytic activity, Water Sci. Technol. 79 (2019) 1494-1502.

Table 1 Comparison of different $Bi_2O_2CO_3$/g-C_3N_4 photocatalytic systems for pollutants degradation.

Pollutant	Concentration (mg L^{-1})	Dosage (mg)	Light source	Time (min)	Removal (%)	Synthesis	Ref.
MO	20	100	500 W W lamp	300	70	Calcination	[71]
RhB	10	50	300 W Xe lamp	100	99	Ultrasonic-assisted	[72]
RhB	8	20	500 W Xe lamp	300	98	Ultrasonic-assisted	[41]
RhB	10	50	500 W Xe lamp	420	99	Planetary milling	[73]
RhB	4.8	50	1000 W Xe lamp	240	46	Calcination	[74]
TCH	44.4	50	300 W Xe lamp	240	98	Calcination	[75]
TCH	10	30	300 W Xe lamp	60	82	Calcination	[67]
TCH	20	20	1000 W Xe lamp	360	96	Hydrothermal	[38]
TCH	10	30	300 W Xe lamp	30	82.6	Hydrothermal	This work

Table 2 The porous parameters of SCN, BOC, and BOC/SCN-3.

Sample	BET surface area ($m^2\ g^{-1}$)	BJH pore volume ($cm^3\ g^{-1}$)	BJH average pore size (nm)
SCN	54.903	0.199	16.145
BOC	16.328	0.089	22.516
BOC/SCN-3	28.846	0.108	16.341

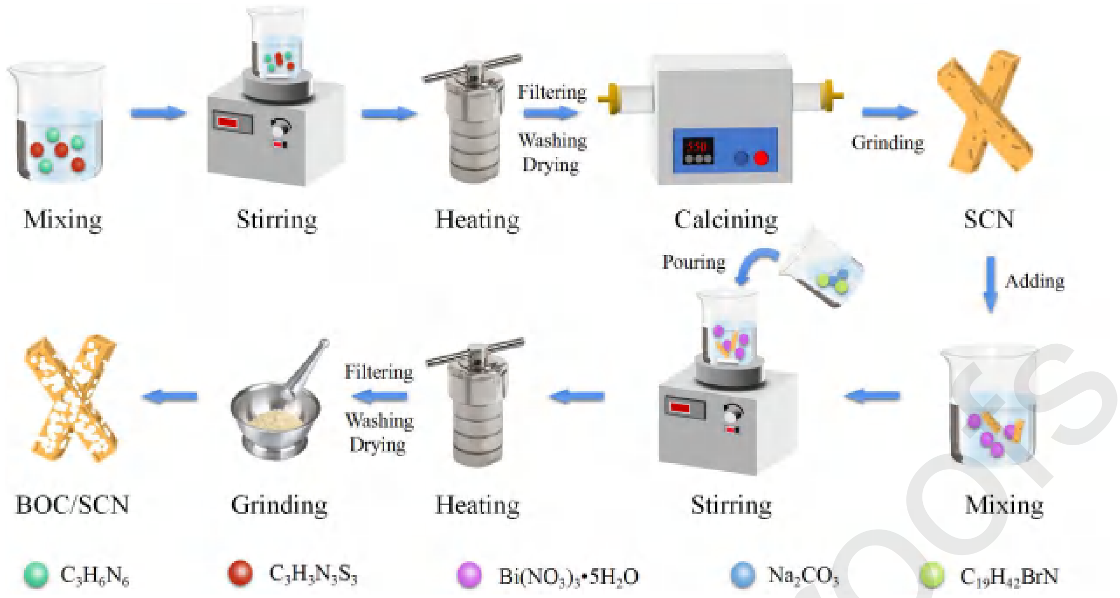

Scheme 1. Illustration for the synthetic process of 2D/1D BOC/SCN composites.

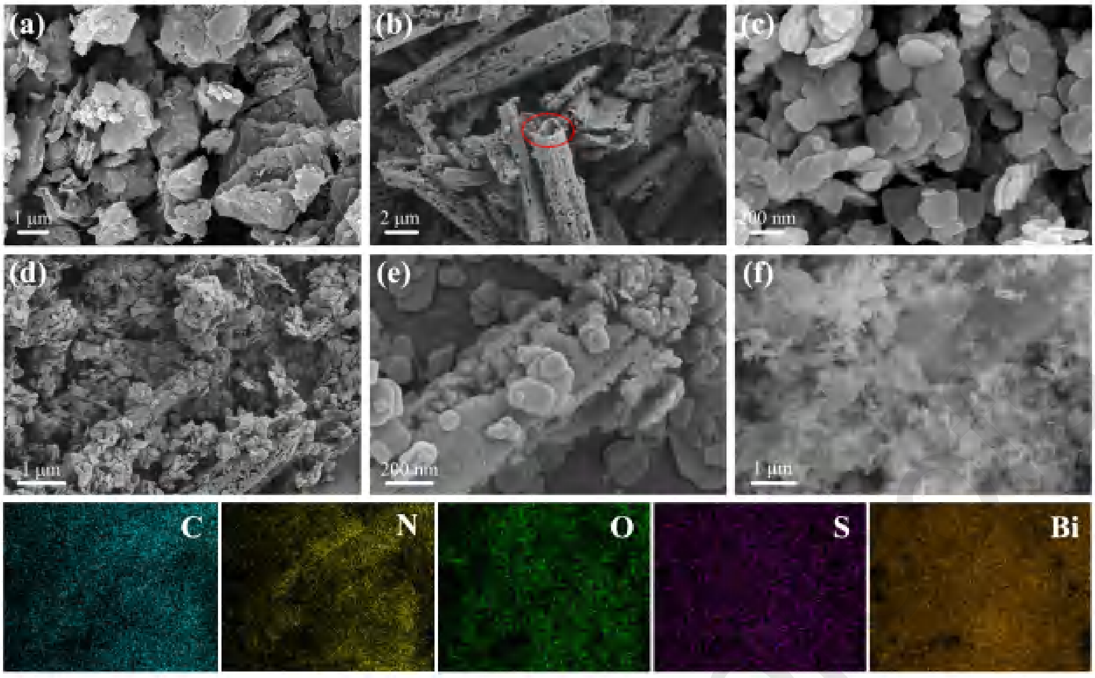

Fig. 1. SEM images of (a) CN, (b) SCN, (c) BOC, (d-e) BOC/SCN-3 and (f) EDX element mapping analysis of BOC/SCN-3.

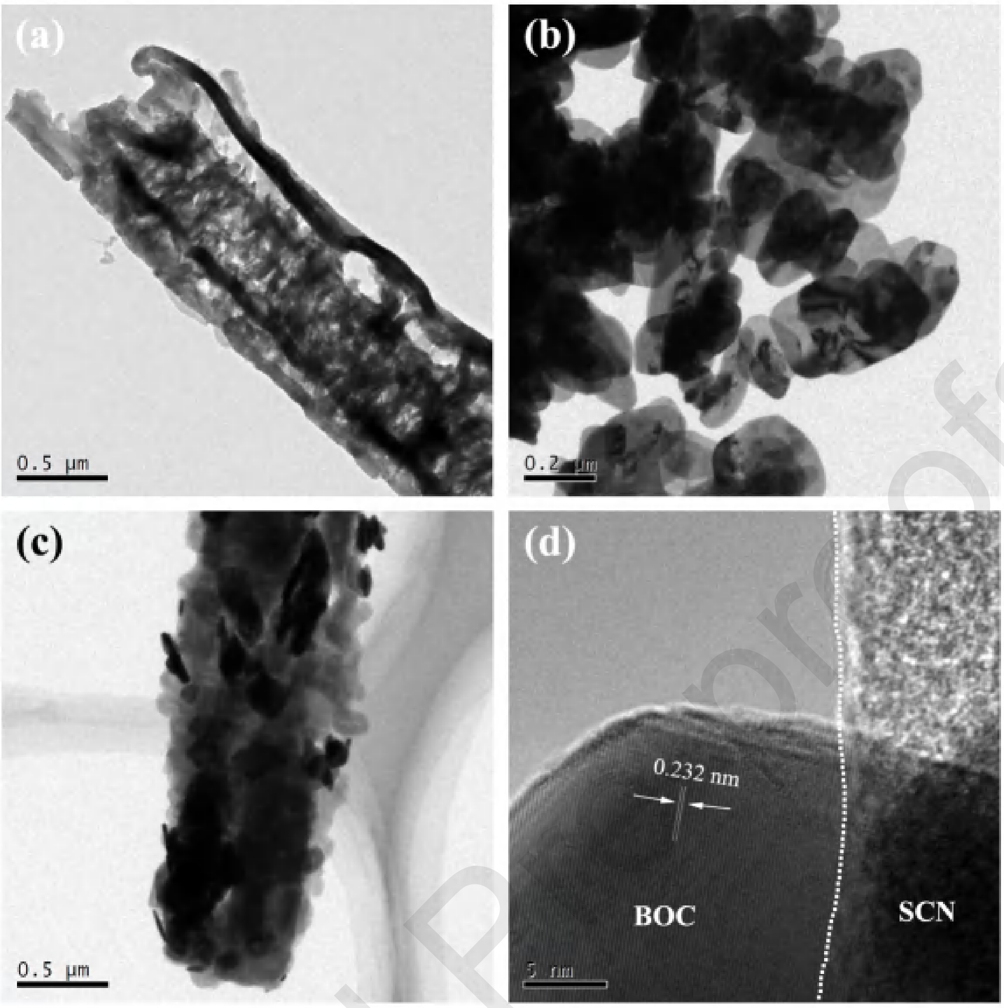

Fig. 2. TEM images of (a) SCN, (b) BOC and (c) BOC/SCN-3; HRTEM image of (d) BOC/SCN-3.

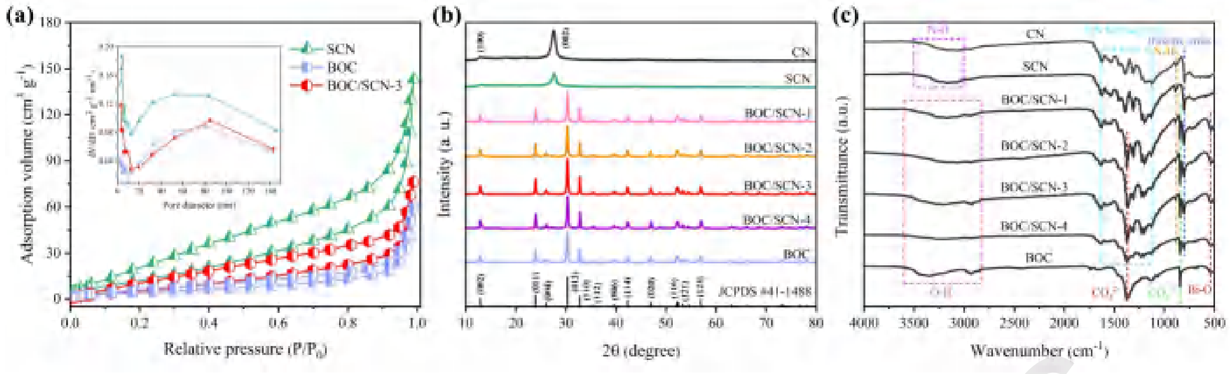

Fig. 3. (a) N_2 adsorption-desorption isotherms of SCN, BOC and BOC/SCN-3 (inset: the related pore size distribution); (b) XRD patterns and (c) FTIR spectra of all the as-prepared samples.

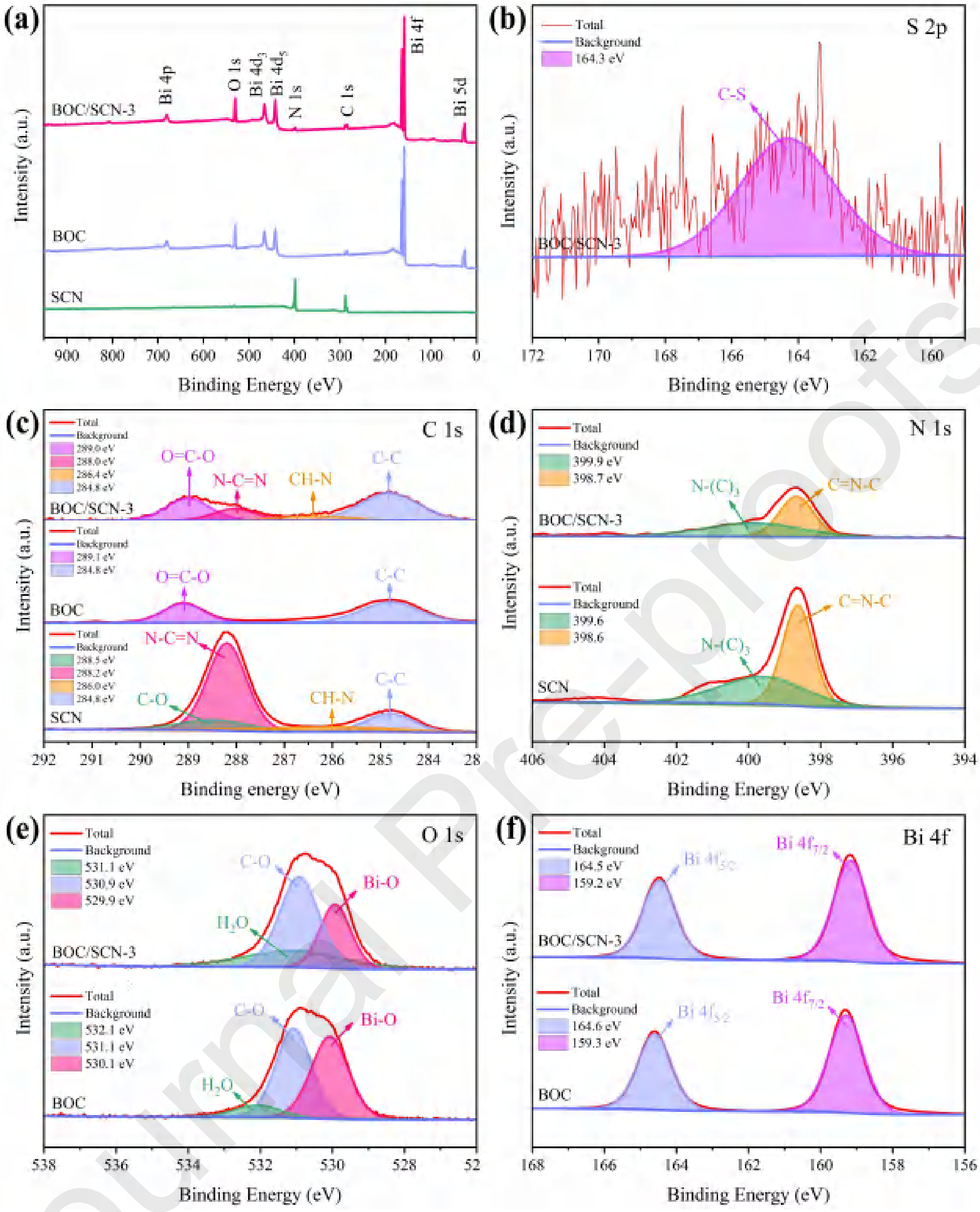

Fig. 4. XPS spectra of SCN, BOC and BOC/SCN-3. (a) Survey, (b) S 2p, (c) C 1s, (d) N 1s, (e) O 1s and (f) Bi 4f.

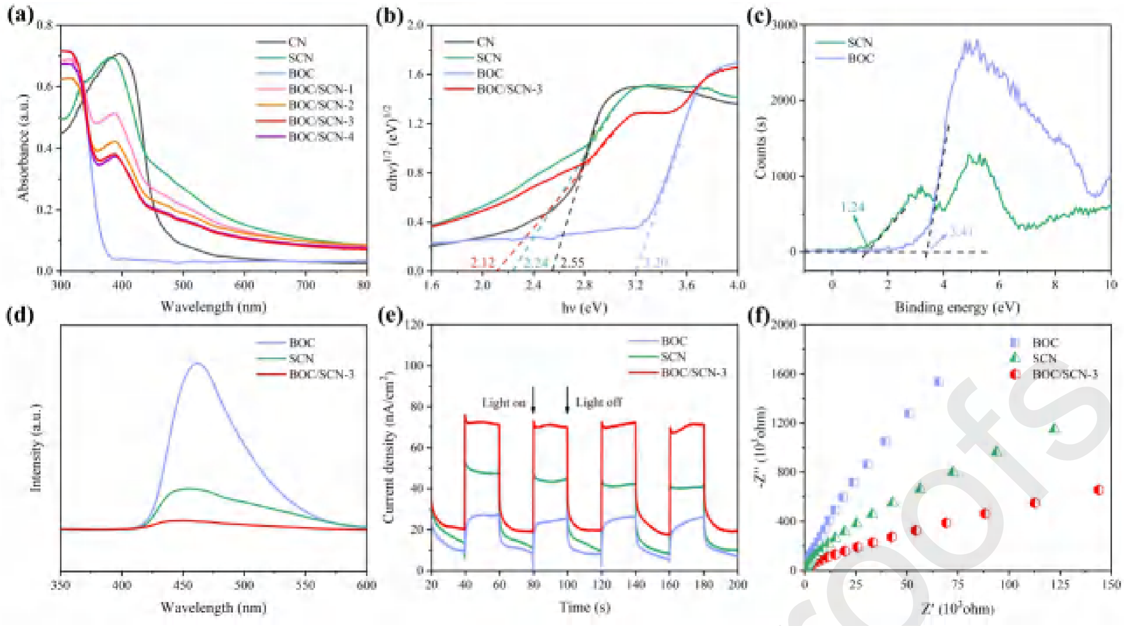

Fig. 5. (a) UV–vis spectra of the as-prepared samples; (b) the bandgaps of CN, SCN, BOC and BOC/SCN-3; (c) the VB-XPS spectra of SCN and BOC; (d-f) PL, photocurrent and EIS of BOC, SCN and BOC/SCN-3, respectively.

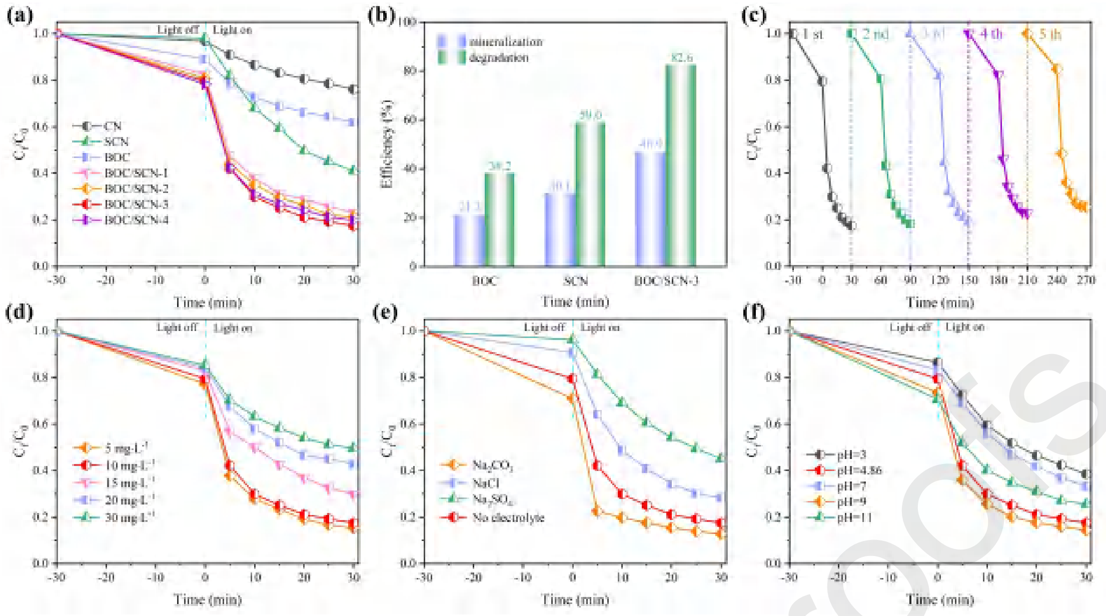

Fig. 6. (a) Photocatalytic TCH degradation of the as-prepared samples under visible light irradiation; (b) mineralization efficiency, (c) recycle experiments and (d-e) effects of initial TCH concentrations, inorganic anions and reaction pH over BOC/SCN-3 for TCH degradation.

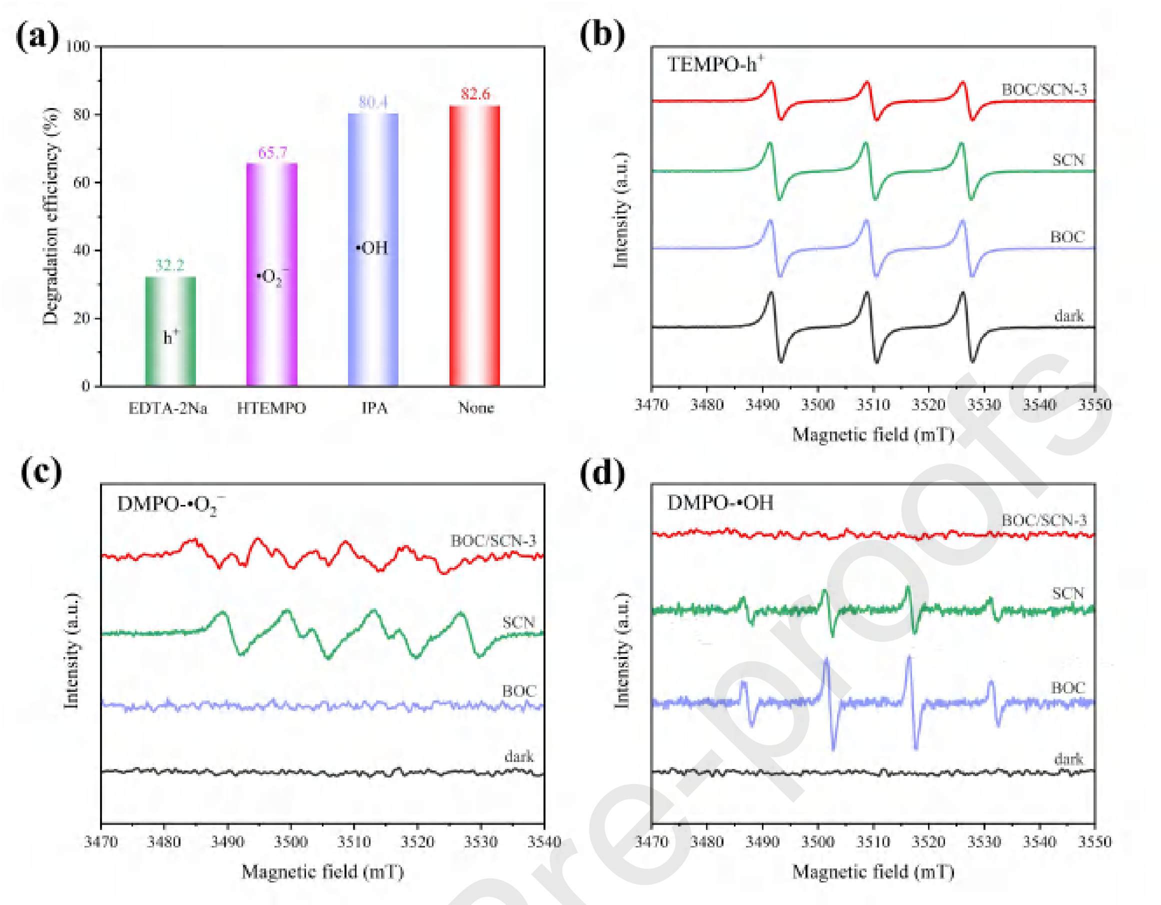

Fig. 7. (a) Radicals trapping experiments over BOC/SCN-3; ESR spectra of SCN, BOC and BOC/SCN-3 at dark and 10 min visible light irradiation conditions: (b) TEMPO-h^+, (c) DMPO-$\bullet O_2^-$ and (d) DMPO-$\bullet$OH.

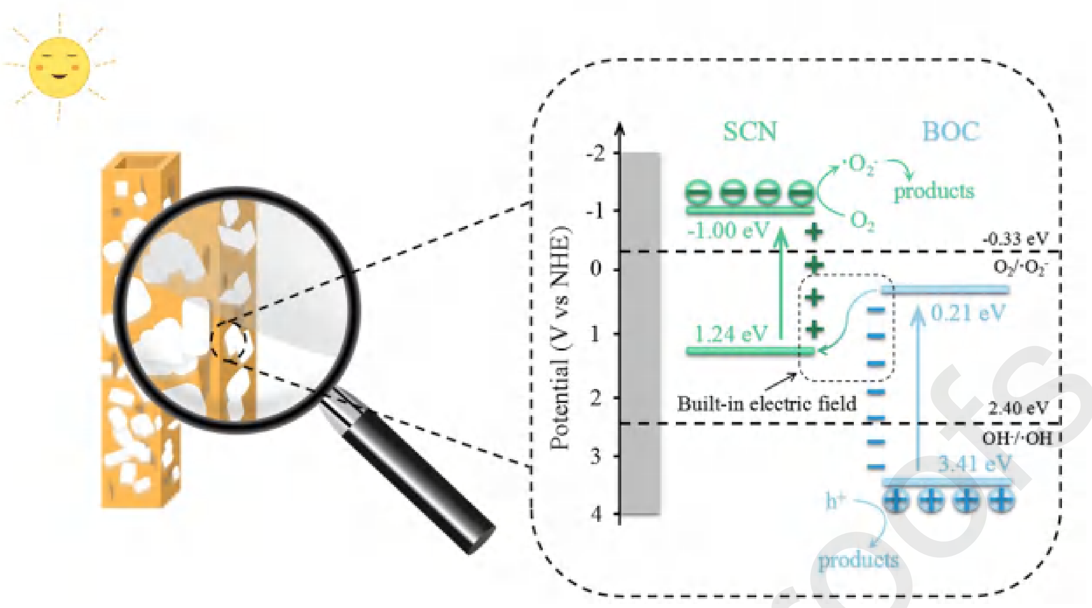

Fig. 8. Schematic illustration of the possible charge transfer pathway and degradation mechanism by BOC/SCN-3 heterojunction.

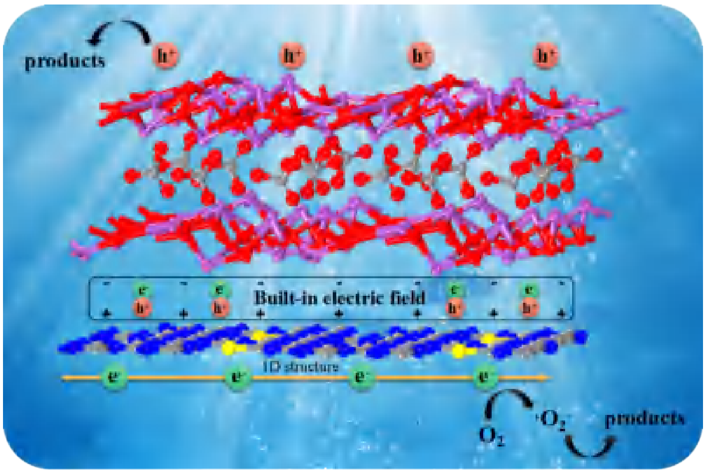

GRAPHIC ABSTRACT

Declaration of interests

☑The authors declare that they have no known competing financial interests or personal relationships that could have appeared to influence the work reported in this paper.

☐The authors declare the following financial interests/personal relationships which may be considered as potential competing interests:

Highlights

- Sulfur doped hollow tubular g-C_3N_4 was prepared through molecular self-assembly.

- A noval 2D/1D BOC/SCN hierarchical heterostructure was constructed.

- BOC/SCN composites exhibited outstanding photocatalytic activity and stability for TCH degradation.

- A possible Z-scheme charge transfer pathway and degradation mechanism were proposed.